

Static and Fatigue Testing of Thick Adhesive Joints for Wind Turbine Blades

Daniel D. Samborsky, Aaron T. Sears and John F. Mandell
*Department of Chemical and Biological Engineering, Montana State University,
Bozeman, MT, 59717, USA*

Ole Kils
*Clipper Windpower Technology, Inc.
6305 Carpinteria Ave.
Carpinteria, CA 93013*

Abstract

Experimental results are presented for the static and fatigue strengths of thick adhesive joint specimens which are representative of blade joints. Four closely related geometries are explored, with over 250 individual tests; fatigue loading conditions include both tension and reversed loading. The four geometries are compared as to static strength statistics and fatigue lifetime trends. Crack origins and crack growth modes are described for each case, along with typical flaws related to the lower strength specimens. Finite element analysis is used to explore interactions between joint geometry, local stress concentrations and pore locations.

I. Introduction

Adhesive bonding and other load transfer details have become issues of increasing importance as wind blade size has increased. Typical blade joints use paste adhesives several millimeters thick, of varying geometry. They can be expected to experience significant static and fatigue loads under various environmental conditions over their service life. The limited data available for joints of this class with metal or composite adherends indicate significant sensitivity to adherend properties and surface preparation, adhesive composition (chemistry, additives, mixing, curing), adhesive thickness, temperature, and moisture, as well as joint geometry. Cyclic fatigue and time dependent creep/stress relaxation are major loading issues, in addition to static loading conditions and multiaxial loads. The variability of joint strength can be greater than that of typical laminates due to a higher sensitivity to flaws such as porosity in the adhesive, poor mixing, unbonded areas or poor dimensional control. Extreme strength issues not generally included in coupon test programs are large areas where the adhesive does not fill the bond gap, and large unbonded or partially bonded areas; these are inspection or structure testing issues.

Joint design and structural adhesives technology have been the subjects of many studies. References 1-5 provide reviews of the structural adhesives literature as it pertains

to fatigue testing, design and lifetime prediction. A series of reports by Tomblin, et. al,^{2,6-8} explore many of the adhesive joint parameters for general aircraft, which are also of relevance to wind blades in many instances. The strengths of lap-shear and many other joint designs for relatively brittle adhesives are dominated by stress concentrations at corners and edges of the adhesive, rather than an average stress condition across the joint.^{1,9,10} The interpretation of test results must consider the stress concentration problem, even if strength data are represented by the average stress across the joint. Because of this problem, the failure of joints is often considered in a fracture mechanics context, with artificial or assumed cracks.^{3,4,12,13}

Failure modes in adhesive joints are broadly represented in the literature^{1,2} as cohesive within the adhesive layer, or interfacial between the adhesive and the adherend; both may be dominated by either shearing or peeling stresses depending on factors such as adherend thickness.² Failure may also occur away from the joint, in the adherend, or in the adherend adjacent to the adhesive. Delamination between plies, particularly the first ply below the adhesive, has been reported as a failure mode for composite adherends.²

The fatigue lifetime of adhesive joints may be determined using the same general test methods as for static strength and fracture mechanics.^{1-7,13-19} Fatigue tests used to determine the lifetime (cycles to failure) of standard test specimen or application oriented geometries, can include a significant component of the lifetime for the initiation of a fatigue crack, followed by a period of crack propagation, until the joint finally separates completely.²⁰ Fracture mechanics based fatigue tests generally measure the growth rate of an artificially induced crack as a function of stress intensity or strain energy release rate loading parameters.^{3,4,13-19} Prediction of joint lifetime using fracture mechanics then requires additional information as to assumed initial and critical flaw sizes, and does not explicitly include crack initiation cycles.^{3,4} A practical approach based on crack growth thresholds determined in a fracture mechanics context might overcome these limitations.²¹⁻²³ Since a significant portion of the fatigue lifetime may be consumed in crack initiation (as for bulk materials), improved joint designs potentially may be based on increasing the crack initiation cycles by prudent choices of adhesive and the details of joint geometry. Thus, particularly for application oriented joint testing, determination of the fatigue resistance of joints which accurately represent the application may be important.

As part of an ongoing study of adhesive bonding for wind turbine blades, this paper reports the results of over 250 static and fatigue tests of specimens prepared by a blade manufacturer. Four specimen geometries were included, all of which are intended to simulate actual blade materials and joint geometries to the extent possible. The test geometries all included adhesive joints on the order of 4 mm thick; limited studies of thickness effects in this range have found reduced joint static and fatigue strength for thick joints in lap shear geometries, which was related to increased eccentricity of the load path²; data for simulated T-geometry intersections showed increased strength for thicker joints, apparently due to increased bending stiffness.²⁰ In neither case was any inherent adhesive strength change due to increasing bond thickness suggested. Tests in the present study were designed to provide adequate data to represent joint strength statistics, fatigue lifetime trends, and representative flaws. Considerable experimental detail and finite element analysis (FEA) results are given for the two more generic

geometries, while less detail is given for the two reinforced (improved) geometries, for proprietary reasons.

II. Experimental Methods

Specimen geometries were based on that given in Figure 1, with either 45° or 90° angles; modified geometries included added reinforcement. The four geometries tested are:

1. Geometry A, 45° wedge block, no reinforcement
2. Geometry B, 90° wedge block, no reinforcement
3. Geometry C, 45° wedge block, with additional reinforcement
4. Geometry D, 90° wedge block, with additional reinforcement

A schematic of Geometry A, 45° with no additional reinforcement, is given in Figure 2, and failed specimens of Geometries A and B are given in Figure 3. Each specimen contained two nominally identical joints, top and bottom in Fig. 1; failure in almost all cases occurred on one side only, with no observable damage to the joint on the other side. All laminates were glass/epoxy with a $\pm 45^\circ$ orientation; reinforcement in the center wedge block was oriented so that the fabric was in the vertical plane, parallel to the load, coplanar with the web adherend. Adhesive thicknesses varied slightly from specimen to specimen, with a nominal value of 4 mm. Specimens were nominally 50 mm wide, with the straight portion of each web 100 mm long. Web thickness was nominally 4 mm for Geometries A and B.

For tensile testing, specimens were loaded by standard hydraulic wedge grips with a grip separation of 185 mm; reversed loading fatigue tests used grip separations of 175 mm (Geometry C) and 75 mm (Geometry D) to avoid buckling. Loads were uniaxial tension or compression. Static tension tests were run at two displacement rates: slow (0.025 mm/s), consistent with test standards, or fast (13 mm/s), consistent with the fatigue rates. Fatigue tests were conducted under sine wave, constant load amplitude conditions at frequencies ranging from 2-4 cycles per second (varied approximately inversely with maximum load, to maintain an approximately constant load rate). Surface temperatures were monitored during selected tests; the maximum temperature rise measured on the adhesive surface was 2 °C. Fatigue loading conditions were either tensile fatigue, $R = 0.1$, or reversed tension-compression, $R = -1$, where R is the ratio of minimum to maximum load for each cycle. Specimens were conditioned and tested at ambient laboratory conditions, approximately 20°C and 30 % R.H.

Although the specimens were slightly unsymmetrical about the load line, out of plane movement during fatigue loading was small. A typical out of plane lateral movement at a load of 25 kN at the mid-height was 0.2 mm for Geometry C.

The adhesive strains were not monitored directly as by shear extensometry,⁷ but the load-deflection curve was determined for Geometry A with an extensometer across the entire joint. The response was moderately nonlinear for the load range used in the static and fatigue tests, but was similar to that for the adherend without a joint. Thus, direct measurements of the strain in the adhesive would be required to characterize the extent of adhesive nonlinearity. A range of conditions have been reported⁸ for paste adhesives in this class for different temperatures and moisture contents, as to adhesive yielding and nonlinearity, for loads which produce fatigue failure in the cycle range of interest in this

study. As described later, failures in this study appeared brittle in character, originating at a flaw or stress concentration.

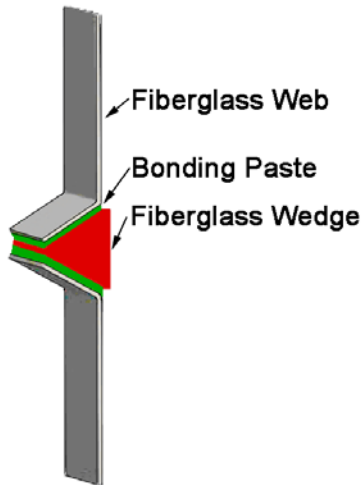


Figure 1. Illustration of simulated blade adhesive joint coupon.

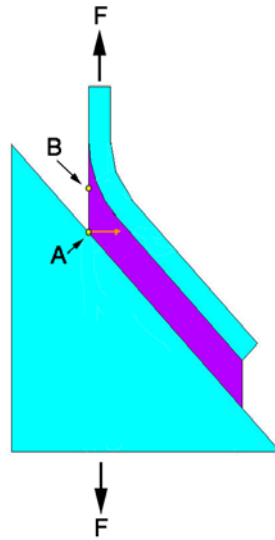


Figure 2. Geometry and location of points of interest and line plot axis.

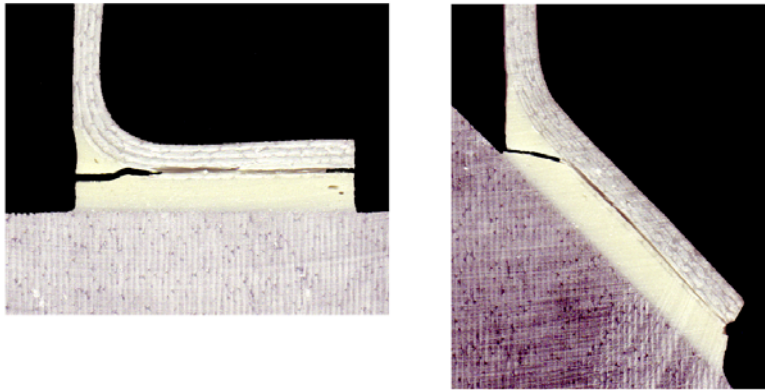


Figure 3. Typical failed specimens of Geometries A (right) and B, edge view.

III. Results and Discussion

A. Static Tests

Table 1 gives the static strength parameters for the four geometries described above. All data are normalized by the mean static strength (failure load per unit width) for Geometry A tested at the slow rate. As noted in Table 1, the number of coupons tested for each geometry was 20 at the slow (test standard) rate and 15 at the fast (fatigue) rate. The number of joint tests was twice these values, due to the doubled joint configuration (Fig. 1). The test-by-test strength variation for each of the geometries is given in Figure 4(a-d). The causes of the strength variations are addressed in detail later, but nearly all static test crack origins and initial growth areas were cohesive, within the adhesive layer. Individual test results will be available in the March, 2009 update of the DOE/MSU Fatigue Database.²⁷

Table 1. Static normalized strength data (normalized by the Geometry A, slow static average strength)

Geometry	Test Rate (mm/s)	Normalized Mean Strength	95/95 Normalized Strength	S.D.	COV (%)	No. Coupons	n
A	0.025	1.00	0.687	0.145	15	20	40
A	12.6	0.956	0.590	0.162	17	15	30
B	0.025	0.977	0.572	0.188	19	20	40
B	12.6	0.940	0.454	0.215	23	15	30
C	0.025	4.06	3.516	0.252	6	20	40
C	12.6	3.89	3.075	0.362	9	15	30
D	0.025	2.86	2.078	0.362	13	20	40
D	12.6	2.77	1.505	0.560	20	15	30

The 95/95 confidence limit is calculated following References 24 and 25 as the one-sided tolerance limit:

$$95/95 \text{ strength} = \text{mean strength} - c_{1-\alpha,\gamma} \text{ S.D.} \quad (1)$$

where S.D. is the standard deviation and the parameter $c_{1-\alpha,\gamma}$ is tabulated in Reference 24 as a function of the confidence level $(1-\alpha)$, probability, γ , and the number of joints, n .

The static data show several trends. The effects of test rate are relatively small, with slightly lower average strengths at the slow rate in each case. Paste adhesives in general are materials with significant time effects inherent to their mechanical response, particularly at temperatures approaching their glass transition temperature,⁸ but this was not evident in this test series.

The statistical content of the data in Table 1 and Figure 4 varies between different geometries. The reinforced geometries (C and D) are significantly higher in average strength and show reduced coefficients of variation compared to the corresponding base geometries (A and B). Coefficients of variation are higher for the 90° specimens of both types (Geometries B and D), compared to the 45° specimens (Geometries A and C). The fast test speed results in slightly higher coefficients of variation than the slow speed for

all geometries (the fast data include only 15 tests compared with 20 for the slow speed, for all geometries).

Of significance is the presence of a few particularly low strength specimens in most data sets, which reduce the 95/95 strength values (Table 1). No data have been censored from the calculations for Table 1, even though the low values may include flaws not representative of blades, such as poorly (hand) mixed adhesive and the occurrence of flaws which intersect the machined ends of the coupons; these could induce three-dimensional stresses not characteristic of the continuous webs in typical blades. The causes of low strength values are discussed in detail in Sections C and D.

Considering the datasets for the unreinforced specimens, the average strength values are very close for Geometries A and B (2.3% lower for B), but the 95/95 strength is 17% lower for B, which contains two results less than 60% and one additional less than 70% of the average. These very low test results are out of the 70 static tests run on the two unreinforced geometries; the total joints tested for these two geometries, due to the doubled configuration with two joints per specimen (Fig. 1), was 140. The two lowest strength values were both associated with poorly cured adhesive areas as discussed later (see Section C). If the lowest strength result for the slow rate, Geometry B, is not included, the average strength becomes equal to that for Geometry A, and the 95/95 strength increases to 0.665. For the reinforced geometries, C and D, Geometry C shows but a single value below 80% of the average for the two test rates combined, while Geometry D shows four values below 70% of the average for D, for the two test rates combined.

The scatter in the data for these test series may reflect variations in the test specimen geometry, mixing of the two part adhesive, porosity, unbonded areas or other factors as discussed later. Other data for paste adhesives using standard types of lap shear geometries show coefficients of variation ranging up to 20%.⁶

B. Fatigue Tests

Fatigue results for the four geometries are presented in Figures 5-7. All fatigue data are plotted as normalized force/width vs. log cycles to failure (complete separation); the normalized force/width is the value of force/width for the particular test divided by the average static failure force/width for Geometry A at the slow rate. Thus, as with Figure 4, all fatigue data are plotted relative to the Geometry A (45°, unreinforced) data. The slow static data are plotted at one cycle for comparison. The mean lifetime for the fatigue data is then fit to the power law in Eq. (1)

$$F/F_0 = A N^B \quad (2)$$

and $B = -1/n \quad (3)$

where F_0 is the slow static average strength for Geometry A, F is the maximum normalized force/width for the individual test, N is the cycles to failure, A is the one-cycle intercept of the curve fit, and B is the fit exponent, which is often expressed as -1 times its inverse, $1/n$, to be consistent with fatigue crack growth literature.²⁶

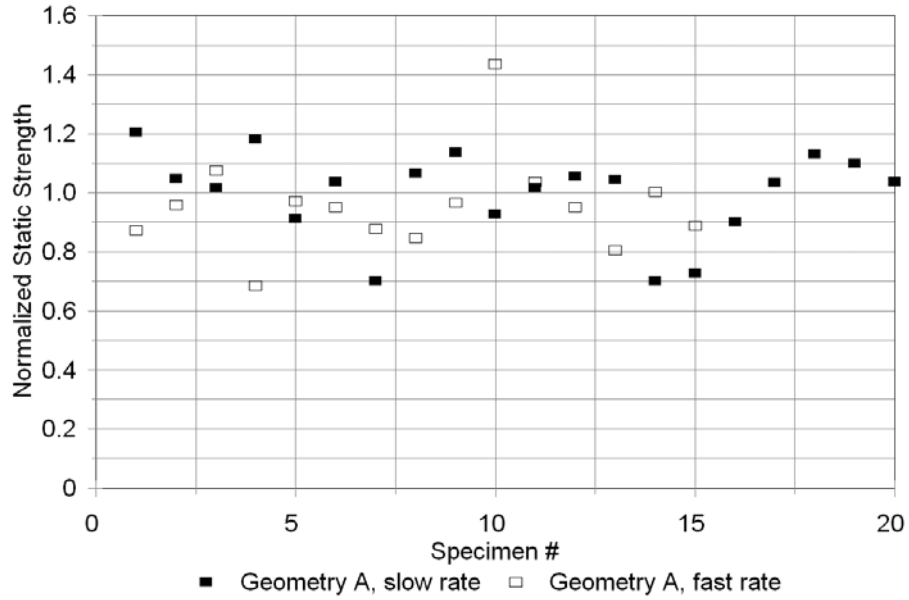


Figure 4. Strength distribution for Geometries A-D, fast and slow test rates, strength normalized by Geometry A slow rate average strength.
Figure 4(a). Static strength, Geometry A.

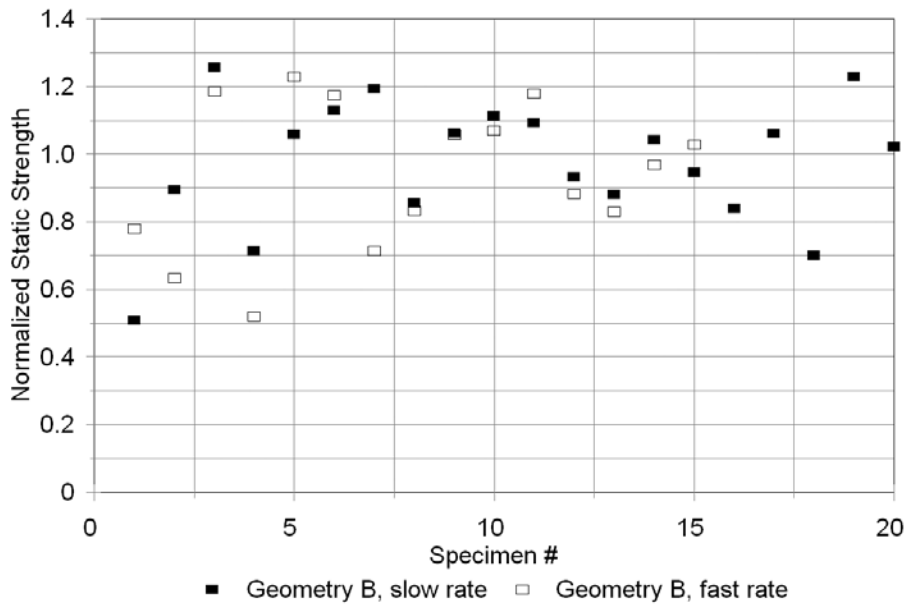


Figure 4(b). Static strength, Geometry B

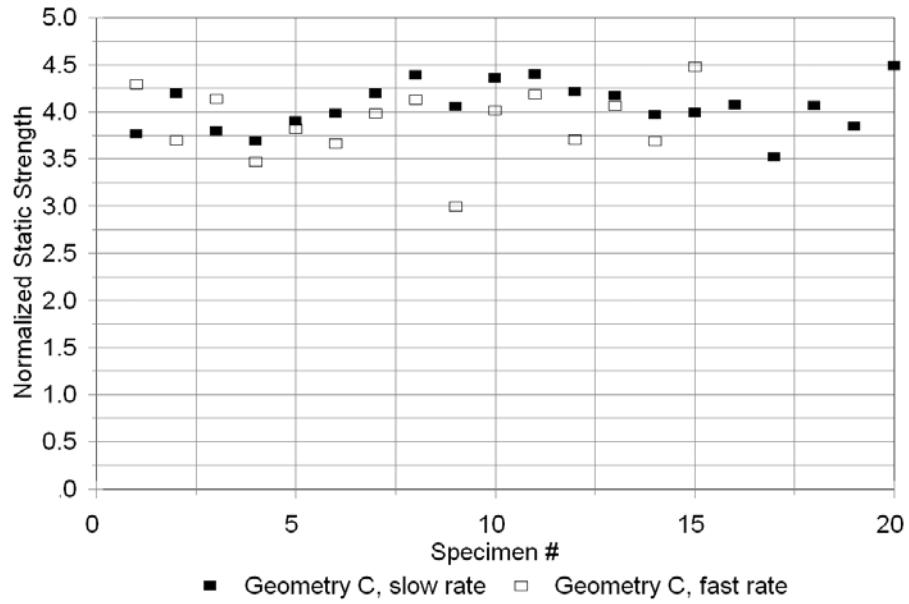


Figure 4(c). Static strength, Geometry C.

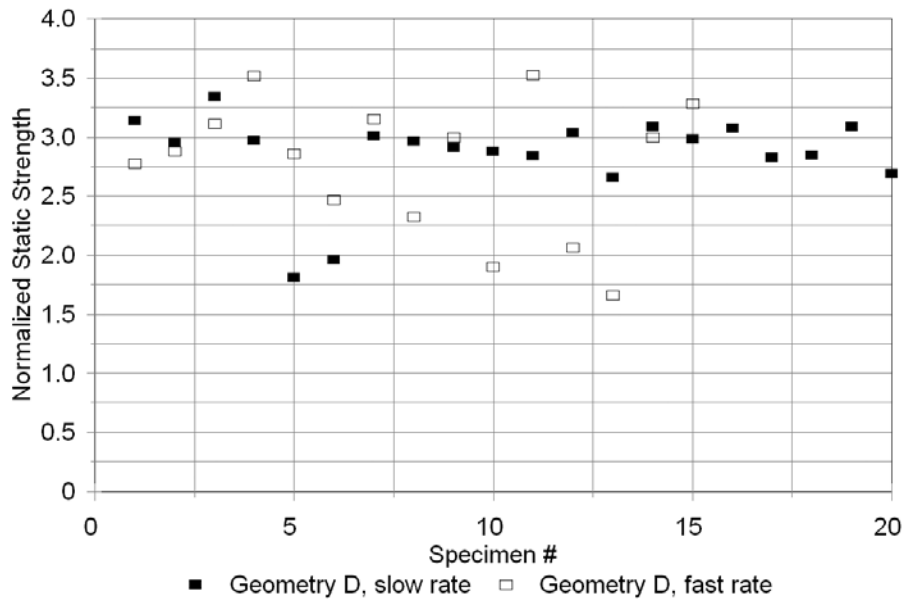


Figure 4(d). Static strength, Geometry D.

The results in Figure 5 indicate little difference in tensile fatigue resistance between the unreinforced Geometries A and B, similar to the static strength results in Table 1. Curve fit parameters given on the figures show similar fatigue exponents for the two cases. Like the static data, the fatigue results show significant scatter. The fatigue exponents, B in Eq. 1, are generally lower than those for typical fiberglass laminates, indicating reduced fatigue sensitivity.²⁸ S-N curve fits were not reported for the only other known fatigue data for thick paste adhesives,⁸ but the fatigue lives for a brittle adhesive system were a similar per cent of the average strength in the 10^5 cycle range to those in Figure 5.

Figure 6 gives tensile and reversed loading results for Geometry C. Like the static data, these results show significantly increased loads and reduced scatter relative to the unreinforced geometries. Fatigue exponents are higher than for Geometries A and B, indicating steeper S-N curves, but still in the range reported for most laminates.²⁸ Results for Geometry D in Figure 7 show reduced exponents but increased scatter relative to Geometry C, consistent with the static data, with one very short lifetime specimen consistent with the low static strength specimens.

The data for reversed loading, $R = -1$, for Geometry C reflect a change in failure mode from cohesive in the adhesive for all other geometry and load cases, to interlaminar in the adherend; the fatigue exponent, B , increases to -0.011 . Under reversed loading Geometry D failed in a manner consistent with the static and tensile fatigue tests. Specimens of Geometries A and B, with thinner web material, could not be tested in reversed loading due to web buckling in compression. The shift to an adherend failure mode for Geometry C is not surprising, since ± 45 laminates like the web used in this study are much less fatigue resistant under reversed loading, apparently due to the full reversal of the internal lamina shear stress direction in the individual 45° plies. Figure 8 illustrates this effect for a typical ± 45 glass/epoxy laminate loaded in-plane, comparing $R = 0.1$, and -1 fatigue datasets as a function of maximum strain (the compression fatigue, $R = 10$ curve, is included for comparison). The exponents, B , for $R = 0.1$ and -1 are both about -0.124 (similar to Geometry C at $R = -1$), but strain levels are much lower for $R = -1$.

Table 2 compares the static strength, fatigue exponent and normalized strength at 10^6 cycles for the four geometries under tensile fatigue. Although the S-N curves are steeper for the reinforced geometries (C and D), these geometries are significantly stronger than the unreinforced geometries over the tested lifetime range.

Table 2. Comparison of static strengths and curve fit parameters for $R = 0.1$ (Eq. 1 and 2), for different geometries.

	Average Normalized* Static Strength	Fatigue Curve Exponent, B	Fatigue Curve Exponent, n	Normalized* Strength At 10^6 Cycles
Geometry A	1.00	-0.0378	26.4	0.385
Geometry B	0.977	-0.0494	20.2	0.383
Geometry C	4.06	-0.0827	12.1	1.73
Geometry D	2.86	-0.0768	13.0	1.27

*Static strengths for the slow test rate, normalized by the average strength for Geometry A; fatigue parameters calculated from the fit equations given on Figs. 5-7.

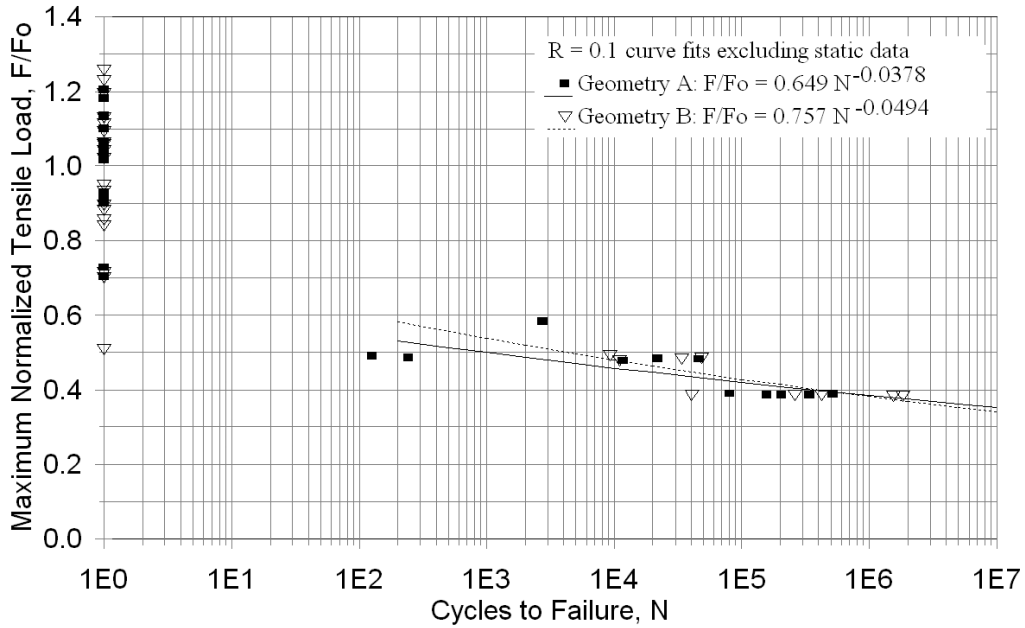


Figure 5. Tensile fatigue data and curve fits for Geometries A and B, R = 0.1, load normalized by the average static failure load for Geometry A, slow rate.

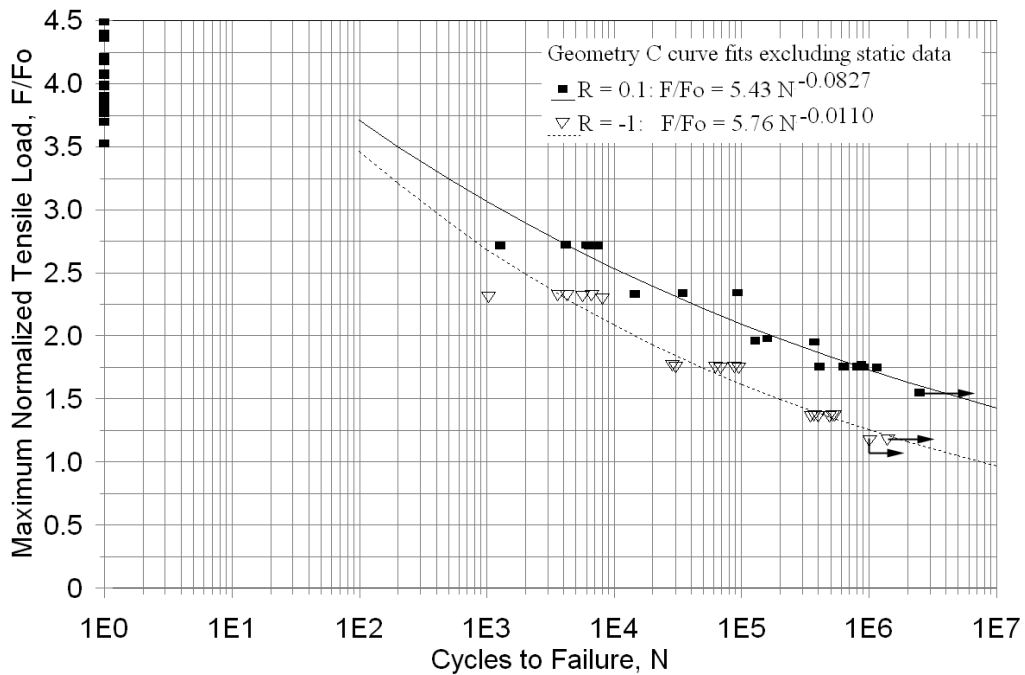


Figure 6. Tensile (R = 0.1) and reversed (R = -1) load fatigue data for Geometry C, load normalized by the average failure load for Geometry A, slow rate.

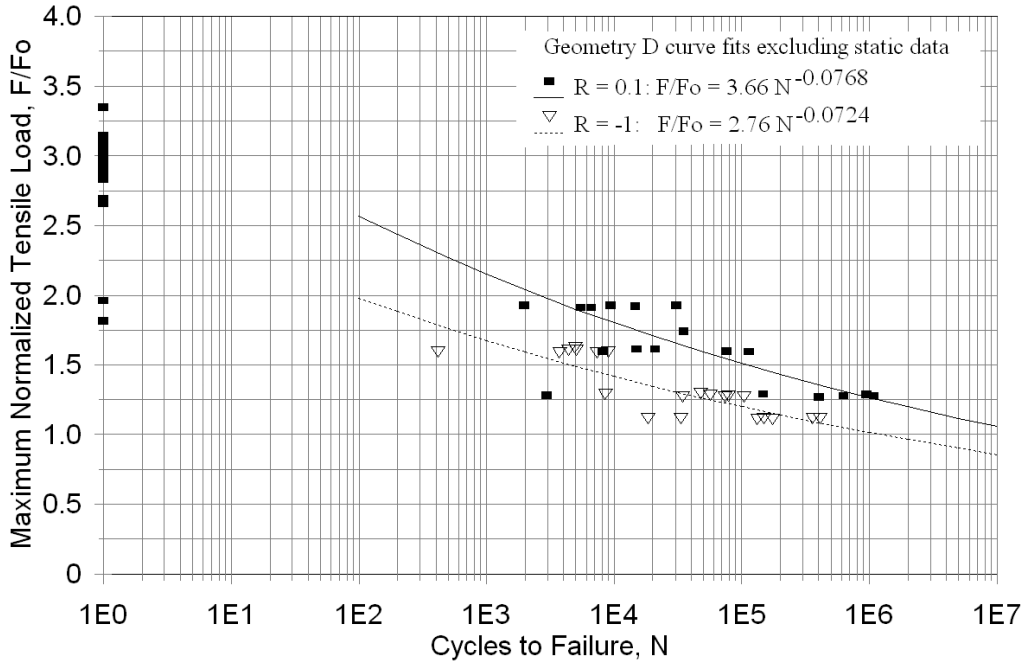


Figure 7. Tensile (R = 0.1) and reversed (R = -1) load fatigue data for Geometry D, Load normalized by the average static load at failure for Geometry A.

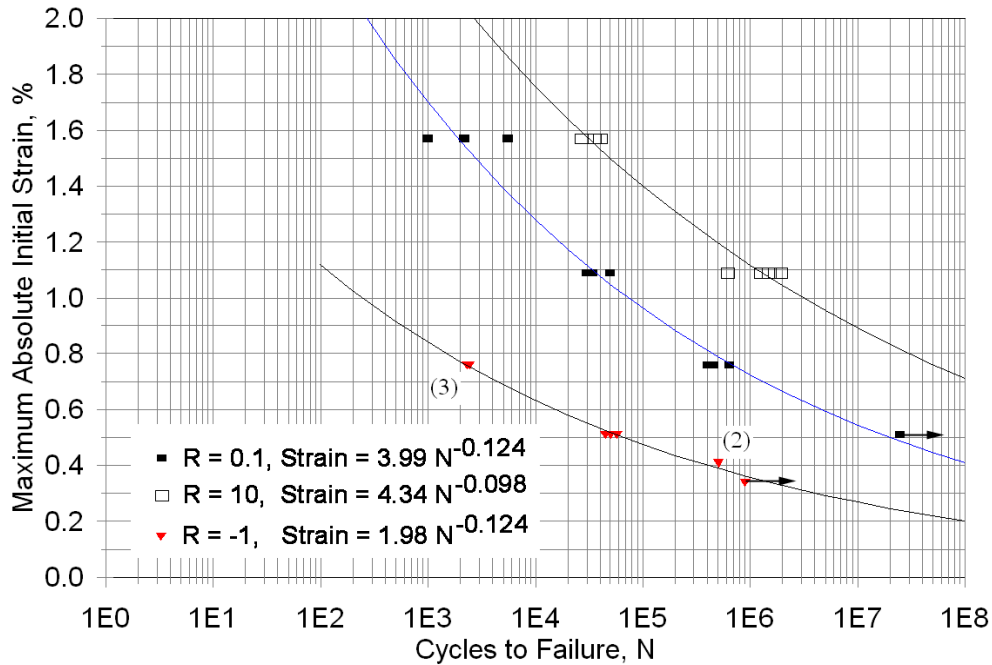


Figure 8. Typical in-plane fatigue S-N curves for ± 45 fiberglass laminate at R = 0.1, -1 and 10; Saertex 830 g/m² fabric with Hexion RIM 135/RIMH 1366 epoxy resin, 45 % fiber by volume.

C. Failure Modes

Failure modes are characterized generally by the position of the crack origin (where it could be determined from fracture surface markings), the position of the crack (cohesive in the adhesive, interfacial between adhesive and adherend, or interlaminar in the adherend)^{1,2} and the position of subsequent propagation of the crack. Stable fatigue cracking could be observed visually, with magnification, during the late stages of many fatigue tests for Geometries C and D. Fracture surfaces also could be interpreted in many cases as to crack initiation sites and the progression of the crack.²⁶ Also described in this section are flaws observed on the fracture surface and on cross-sections of specimens.

Flaws fell into four categories in addition to minor geometric imperfections:

1. pores in the adhesive
2. pores in the adherend near the adhesive interface
3. unbonded or partially bonded areas between the adhesive and adherend
4. partially cured adhesive areas

Virtually all specimens contained visible pores in the adhesive, as reported for other paste adhesives⁸, but most were not involved in the failure process. Unbonded and partially bonded areas were evident as shiny regions on the adherend fracture surface. Partially cured areas also had a distinct appearance on the fracture surface and were often sticky to the touch (adhesive mixing was by hand in small batches, unlike typical blade manufacture, so the partially cured areas may not be representative of blades). Unbonded and partially cured areas were not observed for all geometries; different geometries were fabricated at different times.

Fracture surfaces were studied at low magnification for selected specimens of all four geometries, for specimens having low, average, and high strength and fatigue lifetime. Typical cases of pores at the fracture origin and partially cured areas were found for the weaker specimens for Geometries A and B, shown in Figure 9. Fatigue failure modes were generally similar to static failure modes. Failure for all of the Geometry A specimens started cohesively in the adhesive near Point A, the sharp corner in Figure 2, where there is a significant stress concentration due to the geometry, discussed in the next section. In most cases the crack followed the path shown in Figure 3, propagating across the adhesive, then into the adherend, where it propagated in an interlaminar mode to produce joint separation, similar to literature reports²⁰. A few of the partially cured specimens failed entirely in a cohesive mode in the adhesive (Figure 9). Lower strength values for Geometry A specimens were associated with either poorly cured areas or pores very close to the stress concentration at Point A; typical cases are shown in Figure 9. Since Geometry A specimens usually failed at the sharp corner (Point A, Fig 2), the detailed shape of the corner is also a likely source of variability; the crack origin was often slightly above Point A when the corner was not sharp, as for the strong specimen in Figure 9. This was not analyzed in detail.

Most Geometry B specimens failed in the vicinity of Point B in Figure 2, with the crack again propagating across the adhesive in a cohesive mode, then into the adherend (Figure 3). Crack origins were mostly at pores in this general area. A few poorly cured cases were also found, notably including the lowest strength specimen in both the slow and fast rate datasets. The second weakest specimen in the slow dataset failed at a large pore in the surface of the laminate, adjacent to the adhesive.

Fracture origins for Geometry C and D specimens under static loading were most commonly observed at stress concentration points, mainly adjacent to the wedge block, at pores, or at unbonded areas between the adhesive and adherend; poorly cured adhesive areas were not observed in these geometries. Cracks initially propagated either in a cohesive mode in the adhesive or in an adhesive/cohesive mode near the interface, but usually slightly into the adhesive. As for Geometries A and B, most of the cracks shifted to an interlaminar mode in the adherend for much of their growth. The single low static strength specimen for Geometry C failed from a large unbonded area. Many other specimens with unbonded areas showed near-average strength. The lowest strength specimens for Geometry D were associated with poorly bonded areas adjacent to the wedge block, and appeared interfacial in growth mode.

Fatigue failures for Geometry C were similar to static failure modes at $R = 0.1$, with large fatigue cracks observed in the final stages of lifetime. Evidence of fatigue cracks on the fracture surfaces could be identified from the texture, but with difficulty. The failure mode changed to interlaminar in the adherend under reversed loading, $R = -1$, with large interlaminar fatigue cracks in the adherend observed prior to failure. Fatigue failures for Geometry D generally followed similar modes to the static tests for both R -values. The individual outlier points for each R -value were associated with large, apparently poorly bonded areas on the wedge block surface.



Figure 9. Fracture surfaces of Geometry A specimens, Point A, Figure 2 is at the bottom of the adhesive in each case, with crack propagation toward the top. Left, stronger than average specimen, no major flaws; center, weaker specimen, two large pores along edge of adhesive; right, weakest specimen, poorly cured adhesive (cohesive mode over entire surface).

D. Finite Element Results

Finite element modeling was carried out on Geometries A and B only, to help in understanding some of the experimental trends. As noted earlier, the two geometries were similar in average static strength, but Geometry B showed greater scatter. This result is partly explained by the poorly cured areas of B for the lowest strength specimens, but there also appeared to be added association with porosity. FEA modeling was carried out in plane stress, two dimensions in ANSYS with plane 183, 8-node quadratic elements, with linear elastic assumptions (which is a simplification considering the nonlinearity discussed earlier). Elastic constants for the adhesive were assumed as $E = 2.618$ GPa, $G = 0.971$ GPa, $\nu = 0.35$, and for the adherends, $E_1 = E_2 = 11.7$ GPa, $G_{12} = 3.1$ GPa, and $\nu_{12} =$

0.187. All results are presented for an applied load equal to the average failure load, Geometry A, at the low rate. Figure 2 gives the overall geometry including the sharp corner at Point A which is associated with a high stress concentration. A typical maximum strain map is given in Figure 10, for the maximum tensile strain in the joint. The stress concentration at Point A (Fig. 2) is seen to be extremely localized.

First, the adhesive strain distribution in the absence of flaws is considered. The tensile and shear strains are given in Figures 11 and 12, respectively, for four variations in geometry studied, which included Geometries A (45°) and B (90°), as well as for additional wedge block angles of 30° and 60° . Strains are plotted from Point A, along the line indicated in Figure 2. The assumed sharp corner at Point A results in a mesh dependent maximum strain value as Point A is approached. The closest point plotted on the figures is one element away from Point A. Considering the maximum tensile strain, the results in Figure 11 indicate strains in the vicinity of Point A on the order of twice as high for Geometry A as for Geometry B, suggesting that Geometry B would be significantly stronger. This is contradicted by the observed average experimental static strengths in Table 1, and fatigue strengths in Figure 5, which are similar for Geometries A and B; the reasons for this difference are addressed by considering the effects of pores and failure location.

The most common crack initiation location for Geometry A was Point A in Figure 2, as expected from the local stress concentration. The most common crack initiation location for Geometry B was in a region around Point B in Figure 2, where the strains are lower than at Point A in the absence of an additional stress concentrator. FEA solutions were carried out with several pore sizes, shapes and locations, as depicted in Figure 13, with a typical mesh shown in Figure 14. The variation in maximum tensile strain with distance from Point A, along axis in Figure 2, is given for several pore locations in Figure 15. As the pore approaches Point A, the maximum strain at Point A is seen to increase above the value with no pore present, so that the strength would be expected to drop, but only for pores which are close to Point A. The strain at the edge of the pore remains below the value at Point A until the pore actually intersects the edge of the adhesive. Thus, the effect of pores on the strains in Geometry A is to raise the strain at the geometric strain concentration when the pore is close to the corner. Otherwise, pores have no significant effect on the failure process.

Figures 16 and 17 explore the behavior of Geometry B, which showed about the same average strength as for Geometry A, but with more scatter. As noted above, the strains at the adhesive corner, Point A, are lower than for Geometry A. Failures were usually observed along the area of Point B in Fig. 2, at pores. Figure 15 indicates that the maximum strains for Geometry B shift to the edge of pores in this vicinity. Results in Figure 17 indicate high strains for elliptical pores close to the edge of the adhesive (plotted along a line parallel to the axis in Fig. 1, but starting at Point B). The local strains with pores now appear to be similar to those for Geometry A in Fig. 15. The increased scatter for this geometry is apparently the result of a shift to a more flaw dominated strength, where the presence and variability in severity of pores in the relatively large area around Point B is greater than the variability in geometry and pore incidence near Point A for Geometry A. An accurate prediction of bond strength in both geometries would require more detailed study including nonlinear effects. Prediction of fatigue life would require treatment of the crack initiation process; stable fatigue crack propagation

was not observed for these two geometries in the experiments, but would likely be a significant factor for larger structures and more complex joint geometries, like Geometries C and D.

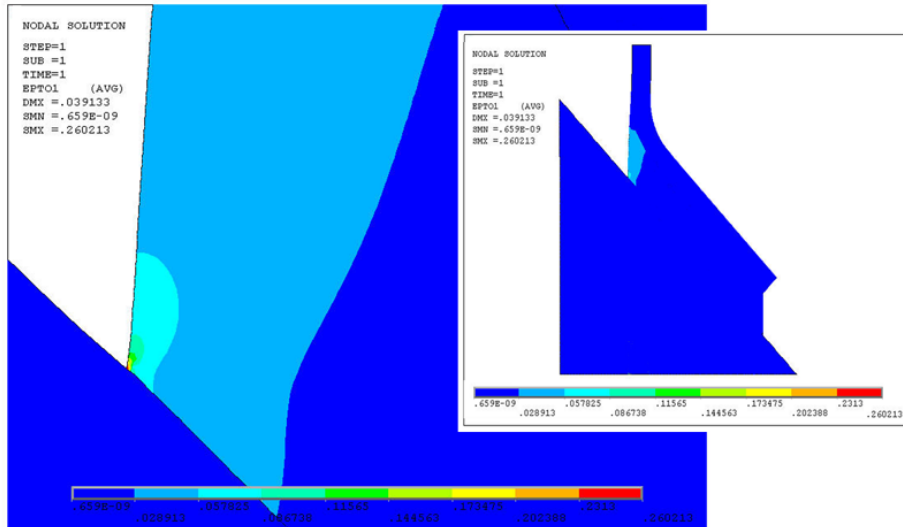


Figure 10. Maximum tensile strain distribution for Geometry A; expanded view shows stress concentration at Point A (Fig. 2).

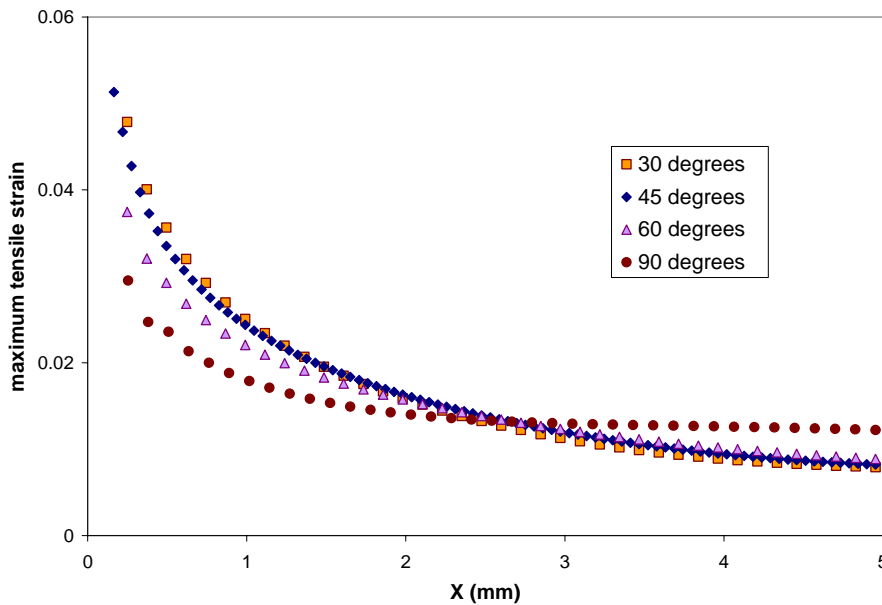


Figure 11. Maximum tensile strain distribution across the adhesive along the x-coordinate at Point A in Fig. 2 for four wedge block angles. Geometries A and B are 45° and 90°, respectively.

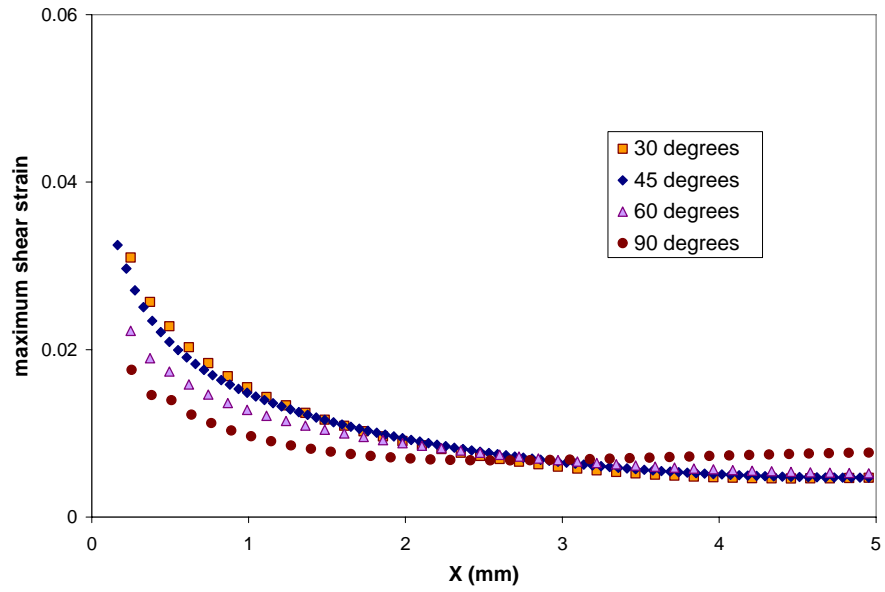


Figure 12. Maximum shear strain distribution corresponding to Fig. 10.

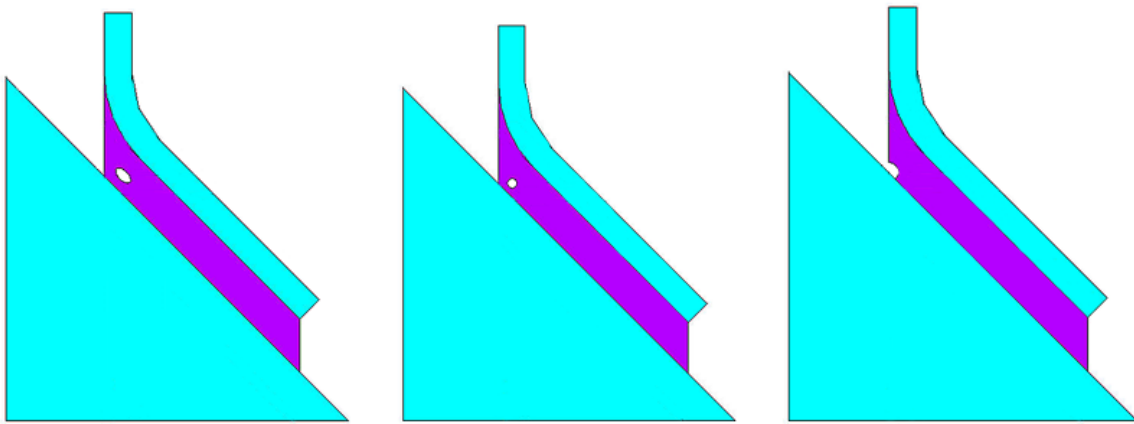


Figure 13 Typical pore geometries, ellipse, circle, intersecting circle.

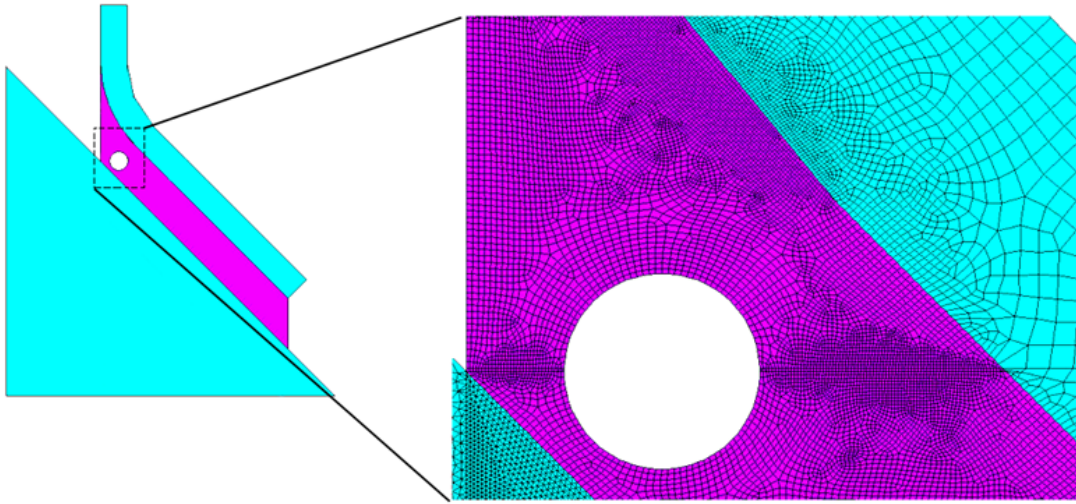


Figure 14 Typical mesh pattern around hole and corner

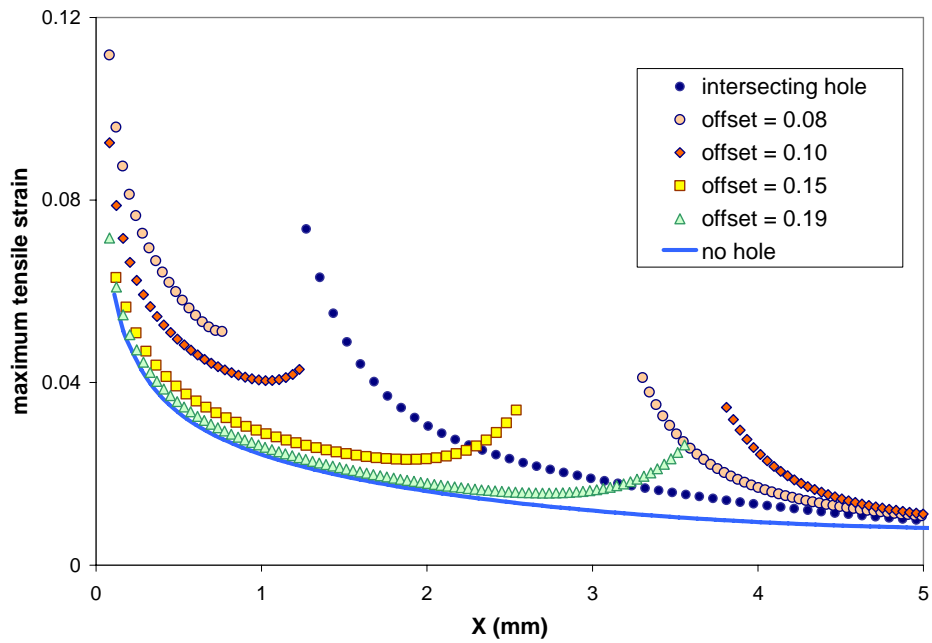


Figure 15. Maximum tensile strain across adhesive along x-coordinate (from Point A in Fig. 2) for 12.5 mm diameter circular pores centered in various positions, Geometry A (offset is the distance to the pore center from $x = 0$; intersecting pore center is at $x = 0$).

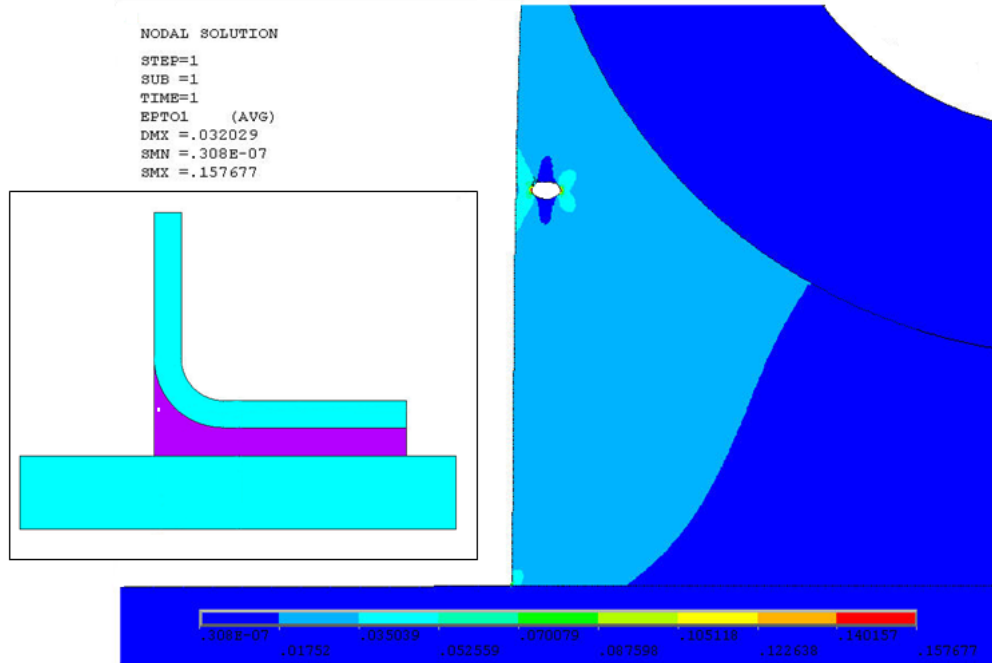


Figure 16. Tensile strain distribution at small elliptical hole in Geometry B specimen near Point B in Fig. 2.

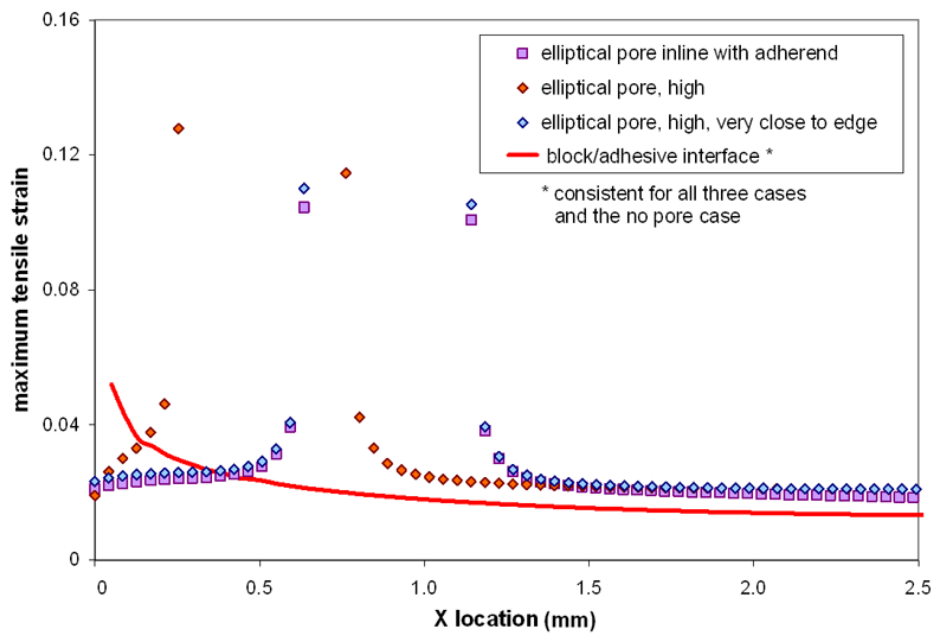


Figure 17. Maximum tensile strain for elliptical holes, Geometry B, plotted along block interface and near Point B in Fig. 2.

IV. Conclusions

Static and fatigue test results have been presented from over 250 tests including four geometries, two static testing rates, and two fatigue loading conditions. The test geometries, fabricated by a blade manufacturer, are representative of typical blade joints using a relatively brittle, thick paste adhesive. Various flaws and failure modes have been identified, and some have been explored with finite element modeling. The following conclusions have been reached:

1. The 140 static test results indicate that the average strengths are similar for Geometries A (45°) and B (90°), while the corresponding reinforced geometries, C and D, are significantly stronger, with lower coefficients of variation. Geometry B produced significantly greater strength scatter than Geometry A, which reduced its 95/95 strength. Most of the difference between Geometries A and B could be related to several poorly cured adhesive specimens. Static strengths were insensitive to differences in test rate (0.025 mm/s vs. 12.6 mm/s).

2. Tensile fatigue results show relatively low fatigue sensitivity in terms of fatigue exponent, for Geometries A and B. Geometries C and D showed somewhat greater sensitivity in terms of fatigue exponent, but fatigue strengths at 10^6 cycles were significantly higher than for the unreinforced geometries. Reversed tension-compression loading produced a shift in failure mode to interlaminar in the adherend, with greater fatigue sensitivity, for Geometry C. This is consistent with the greater fatigue sensitivity under reversed loading relative to tensile loading, of typical $\pm 45^\circ$ laminates used in the adherends. Reversed loading could not be tested for Geometries A and B due to adherend buckling under compressive loads of the thinner adherends.

3. Flaws, crack origins and failure modes were described for each geometry and loading condition, with emphasis on Geometries A and B. Most crack origins and initial growth were cohesive in the adhesive, shifting to interlaminar in the adherend as the cracks extended. For Geometry A, cracks initiated mostly at the major geometric stress concentration, Point A in Fig. 2. Lower strength specimens either contained pores in the adhesive close to Point A or else regions of poorly cured adhesive. Pores were common in most specimens in apparently random locations. Crack initiation in Geometry B specimens was mostly above the stress concentration point, near Point B in Fig. 2; pores could be observed at the crack origin in most cases. Poorly cured adhesive was present in a few specimens of Geometries A and B, including the weakest specimens, apparently related to hand mixing of the adhesive in small batches. Poorly bonded adhesive/adherend interface areas were the most common flaw in weaker specimens of Geometries C and D, where poorly cured adhesive was not observed. As noted above, the failure mode shifted to interlaminar in the adherend for reversed loading with Geometry C.

4. Finite element results showed a significantly higher strain concentration at Point A for Geometry A than for Geometry B. Pores near to Point A in Geometry A increase the strain at Point A, but do not shift the maximum strain location. For Geometry B, failure origins shifted to the edges of pores in the area of Point B in Fig. 2, away from the sharp corner. Maximum strains in these joints are at the pore ends. Joint strength and lifetime for Geometry B are then functions of pore size and location, over a larger volume of the adhesive than for Geometry A, possibly contributing to the increase in scatter.

5. For geometries like A and B, joint strength and lifetime (in the absence of other flaws like poorly cured or poorly bonded areas) is a function of the severity of the geometric strain concentrations inherent to the joint geometry, combined with pore location and severity. If the geometric strain concentration is lower, then failure may be dominated by pores, and dependent on their severity and distribution, possibly leading to increased scatter and reduced 95/95 strength. Changes in adhesive ductility due to adhesive composition or environmental conditions may shift this behavior.⁸

Acknowledgements

This research was supported by Sandia National Laboratories; Dr. Thomas Ashwill was the Technical Monitor.

References

- ¹Petrie, E.M., "Handbook of Adhesives and Sealants, Second Edition," McGraw-Hill, New York, 2007.
- ²Tomblin, J., Harter, P., Seneviratne, W., and Yang, C., "Characterization of Bondline Thickness Effects in Adhesive Joints," J. Composites Tech. and Res., 24:80-92, 2002.
- ³Kinloch, A.J., and Osiyemi, S.O., "Predicting the Fatigue Life of Adhesively-Bonded Joints," J. Adhesion, 43:79-90, 1993.
- ⁴Curley, A.J., Hadavinia, H., Kinloch, A.J. and Taylor, A.C., "Predicting the Service Life of Adhesively - Bonded Joints," Inter. J. Fracture, **103**:41-69, 2000.
- ⁵"Adhesives - Test Methods for Fatigue Properties of Structural Adhesives in Tensile Shear," ISO Standard 9664:1993(E).
- ⁶Tomblin, J., Yang, C. and Harter, P., "Investigation of Thick Bondline Adhesive Joints," FAA Report DOT/FAA/AR-01/33, June, 2001.
- ⁷Tomblin, J., Seneviratne, W., Escobar, P. and Yap, Y., "Shear Stress-Strain Data for Structural Adhesives," FAA Report DOE/FAA/AR-02/97, November, 2002.
- ⁸Tomblin, J., Seneviratne, W., Escobar, P. and Yap, Y., "Fatigue and Stress Relaxation of Adhesives in Bonded Joints," FAA Report DOE/FAA/AR-03/56, October, 2003.
- ⁹Goland, M. and Reissner, E., "The Stresses in Cemented Joints," J. Appl. Mechanics, 11:17-27, 1944.
- ¹⁰Hart-Smith, L.J., "Developments in Adhesives 2," Kinloch, A.J., ed., Applied Science Publications, London, 1981.
- ¹¹Sancaktar, E., "Fracture Aspects of Adhesive Joints: Material, Fatigue, Interphase and Stress Concentrations," J. Adhesion Sci. and Tech., **9**:119-147, 1995.
- ¹²Ripling, E.J., Mostovoy, S. and Patric, R.L., "Application of Fracture Mechanics to Adhesive Joints," Adhesion, ASTM STP 360, ASTM, Phil., p.5, 1963.
- ¹³Johnson, W.S. and Mall, S., "A Fracture Mechanics Approach to Designing Adhesively Bonded Joints," NASA Technical Memorandum 85694, NTIS, Springfield, VA, 1983.
- ¹⁴Jablonski, D. A., "Fatigue Crack Growth in Structural Adhesives," J. Adhesion, **11**:125-143, 1980.
- ¹⁵Luckyram, J. and Vardy, A. E., "Fatigue Performance of Two Structural Adhesives," J. Adhesion, **26**:273-291, 1988.
- ¹⁶Harris, J.A. and Fay, P.A., "Fatigue Life Evaluation of Structural Adhesives for Automotive Applications," **12**:9-18, 1992.

- ¹⁷Metzinger, K. E. and Guess, T. R., "Single Cycle and Fatigue Strengths of Adhesively Bonded Lap Joints," 1999 ASME Wind Energy Symposium, AIAA/ASME, 1999, pp 21-31.
- ¹⁸Sancaktar, E., "Fatigue and Fracture Mechanics," *Engineered Materials Handbook, Vol. 3, Adhesives and Sealants*, p. 501, ASM International, Materials Park OH, 1990.
- ¹⁹Sancatar, E., "Mixed-Mode Fatigue Failure in Structural Adhesives," *Fatigue and Fracture Mechanics: Twenty-Ninth Volume, ASTM STP 1332*, T. L. Panontin and S. D. Sheppard, Eds., American Society for Testing and Materials, West Conshohocken PA, 1999.
- ²⁰Quaresimin, M. and Ricotta, M., "Fatigue Behavior and Damage Evolution of Single Lap Bonded Joints in Composite Material," *Composites Science and Technology*, ⁶⁶:176-187, 2006.
- ²¹Broughton, W.R. and Mera, R.D., "Review of Life Prediction Methodology and Adhesive Joint Design and Analysis Software," National Physical Laboratory, London, June 1997.
- ²²Mandell, J.F., Cairns, D.C., Samborsky, D.D., Morehead, R. B. and Haugen, D.J., "Prediction of Delamination in Wind Turbine Blade Structural Details," *ASME J. Sol. Energy Eng.*, 125:522-530, 2003.
- ²³Ashcroft, I.A. and Shaw, S.J., "Mode I Fracture of Epoxy Bonded Composite Joints 2. Fatigue Loading," *Internat. J. Adhesion and Adhesives*, **22**,151-167, 2002.
- ²⁴Natrella, M. G., "Experimental Statistics," *National Bureau of Standards Handbook 91*, National Bureau of Standards, Gaithersburg, MD, August, 1963.
- ²⁵Sutherland, H. J. and Mandell, J. F., "Optimized Goodman Diagram for the analysis of Fiberglass Composites Used in Wind Turbine Blades," *ASME J. Solar Energy Engineering*, 127:563-569, 2005
- ²⁶Broek, D., *Elementary Fracture Mechanics*, p. 276, Martinus Nijhoff Publishers, Dordrecht, The Netherlands, 1982.
- ²⁷Mandell, J. F. and Samborsky, D. D. "DOE/MSU Fatigue of Composite Materials Database, 2008 Update," (www.sandia.gov/wind/other/973002upd0308.pdf)
- ²⁸Mandell, J. F., Samborsky, D. D. and Agastra, P. "Composite Materials Fatigue Issues in Wind Turbine Blade Construction," SAMPE 2008, Long Beach, May 18-22, 2008.